Article

Oblique pancake bouncing

Ran Tao, Guoqiang Liang, Binhong Dou, Jun Wu, Bing Li, Chonglei Hao

haoc@hit.edu.cn

Highlights

Contact time reduction and droplet directional transport are achieved simultaneously

Flexibility to manipulate oblique pancake bouncing behavior by varying impact velocity

Robust water repellency and liquid motion directionality under various conditions
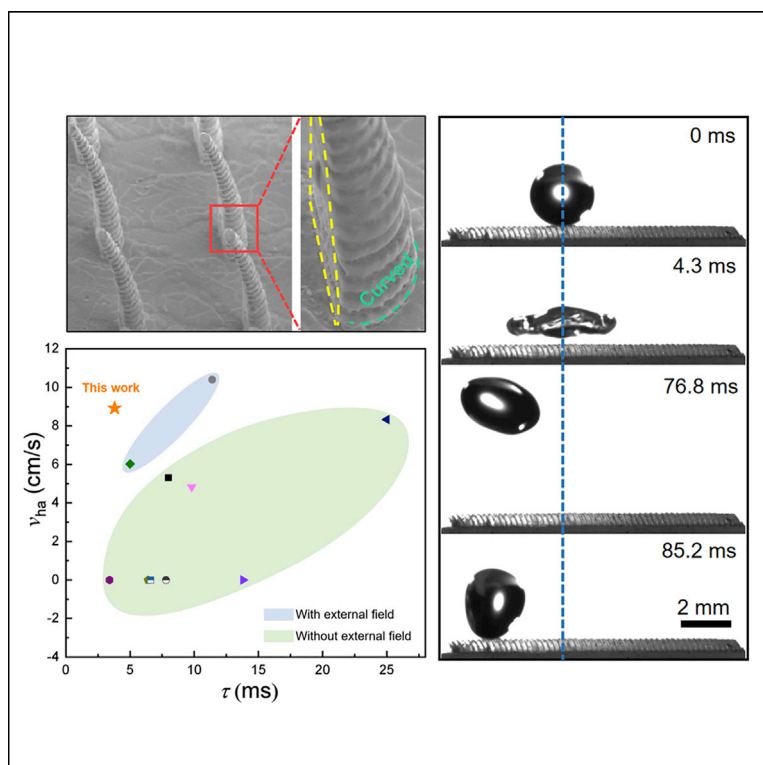
Tao et al. report a strategy to achieve the oblique pancake bouncing of droplets, allowing for a synchronized solid-liquid contact time reduction and the directional transport. Furthermore, the remarkable bouncing performance is applicable to a broad range of working environments with various thermal conditions and impact velocities.

Article

Oblique pancake bouncing

Ran Tao,[1,2] Guoqiang Liang,[1,2] Binhong Dou,[1] Jun Wu,[1] Bing Li,[1] and Chonglei Hao[1,3,*]

SUMMARY

Despite extensive efforts in approaching the theoretical limit of solid-liquid contact time, the vertical bouncing droplet eventually lands on the impact spot of horizontally placed surfaces, which makes the liquid removal inefficient and thus limits its practical applications. To address this challenge, we use superhydrophobic surfaces consisting of regularly patterned pillars with an inclined Janus structure and report a phenomenon that involves synergistic effects of both pancake rebound and directional transport in one bouncing cycle, contributing to the reduction of contact time and the lateral removal of impacting droplets simultaneously. We generalize this particular regime to a broad range of working environments with various thermal conditions and impact velocities, demonstrating the robustness of water repellency and the directionality of liquid motion. The unusual bouncing performance, generality, and practicability of our work may provide useful insights into various applications, including electricity generation, self-cleaning, defogging, and anti-icing.

INTRODUCTION

Liquid drop impingement is pervasive in both nature and industrial technologies, ranging from raindrops falling to spray cooling, inkjet printing, and droplet-based energy harvesting.[1–6] In a typical droplet impingement process, the liquid-solid interaction is governed by an intricate interplay involving surface architectures (e.g., wettability and morphology), impact parameters (e.g., droplet size and velocities), and liquid properties (e.g., density, liquid viscosity, and surface tension).[7] Such a complex interplay thereby shapes various droplet impact dynamics, including splashing, spreading, receding, and bouncing.[8,9] The diverse impact dynamics, in turn, endows fascinating interfacial phenomena and facilitates liquid manipulation. In particular, the rapid detachment of droplets, which is highly associated with spreading and receding, has blossomed in recent decades because of its promising applications in fields of self-cleaning,[10–12] dropwise condensation,[13,14] electrical generation,[15] anti-fogging,[16,17] and anti-icing.[18,19]

Generally, the droplet detachment is quantified by the contact time τ, which is defined as the time interval from the moment a droplet first touches the substrate to its complete bouncing off. Previous research indicated that the impinging drop is analogous to a free oscillation system, so the contact time is dependent on the inertia-capillary time scaled as $\tau \sim (\rho D_0^3/\gamma)^{1/2}$, where ρ, D_0, and γ represent the mass density of the liquid, droplet diameter, and liquid surface tension, respectively.[20,21] As the contact time is a crucial factor in determining the efficiency of mass, momentum, and energy transfer between the liquid and the underlying solid, it is highly desirable to minimize it in practical applications.[22] To achieve this goal, many efforts have been devoted to reducing the contact time. Bird et al. showed

[1]School of Mechanical Engineering and Automation, Harbin Institute of Technology, Shenzhen 518055, China

[2]These authors contributed equally

[3]Lead contact

*Correspondence: haoc@hit.edu.cn

https://doi.org/10.1016/j.xcrp.2021.100721

that the contact time could be reduced by 37% via decorating a superhydrophobic surface with macroscopic ridges and thus triggering a fast droplet retraction.[23] Other attempts have been made to use strategies such as employing surfaces with curvatures, point-like macrotextures, compact nanoscale structures, and delicate-designed post arrays for droplet bouncing to reduce the contact time.[24–27] Among those strategies, the conical-pillar-arrays-induced pancake bouncing is noteworthy since it has substantially reduced the contact time by about 80%.[25] Despite significant progress, the bouncing droplet eventually falls back to the original impact spot owing to the gravity if the substrate is horizontally placed. This indicates that merely reducing the contact time is not an efficient and practical way for droplet detachment. To tackle this challenge, a directional removal after droplet rebound is expected.

Directional liquid transport, which is another active research topic of interfacial hydrodynamics, has been attracting increasing attention. At the early stage, liquid transports are accomplished by external actuations, such as pressure, light, temperature, and electric charge.[28–32] However, this necessitates continuous energy input, makes integration cumbersome, and brings reliability issues. Remarkably, many living organisms achieve the directional liquid motion by leveraging their unique topological characteristics.[33–35] Motivated by nature, various engineered surfaces with delicate structures (e.g., asymmetric microstructures, structural curvature, inclined angle, non-uniform thickness, stiffness gradient, and their combinations) have been fabricated to break the three phase contact lines and thereby introduce direction-dependent energy barriers.[35–37] Fortunately, this perfectly addressed the above problems and gained popularity for the directional flow.[38,39] Therefore, contact time reduction along with a directional liquid bouncing, if it can be easily achieved, will have significant impacts on various areas.

In this work, we report the design of a unique surface consisting of regularly patterned pillars with an inclined Janus structure. On such a surface, the impacting droplet exhibits the typical pancake bouncing, which dramatically reduces the contact time, and it is also accompanied by the directional motion simultaneously, altogether rendering an efficient droplet detachment from engineered surfaces. Finally, it is manifested that the synchronized pancake bouncing with the preferential motion is attainable in a wide range of temperature and impact velocity conditions, which ensures a robust water repellency and liquid flow directionality.

RESULTS AND DISCUSSION

Characterization of oblique pancake bouncing

Our surface consists of regularly patterned pillars of the inclined Janus structure, which is composed of a curved and a flat face (Figures 1A and 1C), while its counterpart is decorated with pillars of inclined conical structure (Figures 1B and 1D). The schematic diagrams of 3D printed samples are depicted in Figures 1E and 1F, where h represents the height of pillars, R_b indicates the base radius, β is the angle between the bottom surface and the pillars' centerline, d is the center-to-center spacing between pillars, α_L is the angle between the left side generatrix of the cone and the bottom surface (for conical structure only), and α_R is the angle between the right side generatrix of the cone and the bottom surface (for both the conical and the Janus structures). We also fabricated control samples by altering geometric parameters, such as h, d, and β, as well as the surface wettability. The geometric parameters and relevant descriptions for all surfaces used in this work are listed in Table 1. The fabrication details are shown in the Experimental procedures section.
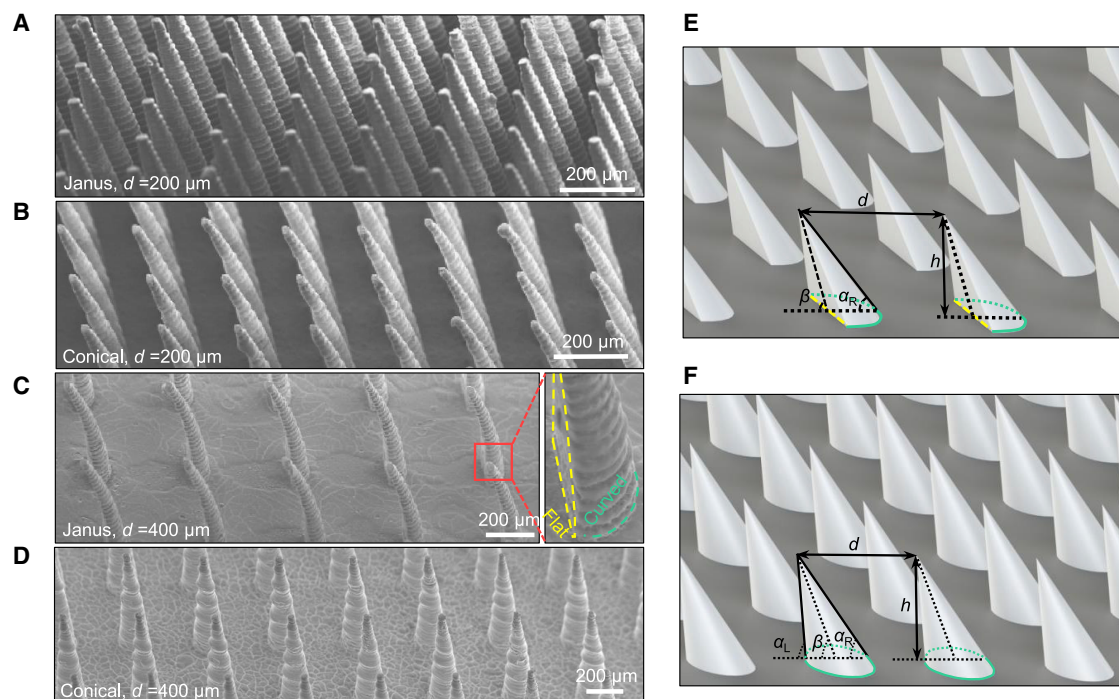
Figure 1. Surface structure characterization

(A–D) Scanning electron microscope (SEM) images showing the surface with (A) Janus structures with d = 200 μm, (B) conical structures with d = 200 μm, (C) Janus structures with d = 400 μm, and (D) conical structures with d = 400 μm. The Janus structure consists of a curved and a flat face. (C) and (D) are shown in order to demonstrate the structures clearly.

(E and F) Schematic drawing showing surfaces with the (E) Janus structure and (F) conical structure.

On the superhydrophobic control surface, the water droplet demonstrates a typical vertical bouncing, as shown in Figure S1. Here, the Weber number is $We = \rho D_0 v^2 / \gamma$, where v is the droplet impact velocity. The measured contact time is about 14.8 ms, which is in good agreement with previous work.[20,21,40] Distinct from that, on the conventional superhydrophobic surface, the droplet on surfaces I–IV (i.e., Janus and conical structures with d = 200 μm) manifests a pancake bouncing, as shown in Figure S2. In such a way, the solid-liquid contact time is substantially reduced to 3.4 ms. Moreover, the pancake bouncing appears only when We > We_c (We_c indicating a critical We), whereas it goes back to the conventional bouncing in the regime of We < We_c (Figure S3). The details of pancake bouncing characterization can be found in Note S1 and Figure S4.

For cases of We > We_c, part of the liquid penetrates the spacing between pillars after impact owing to the downward momentum. Subject to a capillary force applied by the periphery of superhydrophobic pillars, the infiltrated liquid experiences the deceleration, rest, and, finally, upward moving (Figure S2). In this way, nanoparticle-decorated pillar configurations serve as an energy storage device, in which the kinetic energy is converted to the surface energy during the penetration period while the surface energy is released and turns back to the kinetic energy in the capillary emptying process. In the whole process, the capillary force F_c acts as either the resistance force for the downward flow motion or the driving force for the upward liquid motion, which is scaled as $F_c \sim \gamma R_b h_p D_0^2 / (h d^2)$. Here, D_0^2 / d^2 indicates the number of pillars wetted, and h_p is the penetration depth of the impacting droplet.

Table 1. Geometric parameters of surfaces used in this study

Surfaces	Spacing d (µm)	Inclined angle 90-β (°)	Height h (µm)	Morphology
I	200	20	400	Janus structure
II	200	20	400	conical structure
III	200	s0	400	Janus structure
IV	200	0	400	conical structure
V	400	20	400	Janus structure
VI	400	20	400	conical structure
VII	400	0	400	Janus structure
VIII	400	0	400	conical structure
IX	200	20	300	Janus structure
X	200	20	200	Janus structure
XI	200	20	100	Janus structure
XII	200	20	400	Janus structure with a superhydrophilic film
XIII	–	–	–	glass with superhydrophobic nanoparticles

For surfaces I–XII, the base radius R_b is 80 µm.

More importantly, the unique pancake bouncing accompanied by directional liquid transport is observed. Figures 2A and 2B depict selected images of droplet bouncing dynamics on the inclined ($\beta = 70°$, surface I) and vertical ($\beta = 90°$, surface III) Janus structures, respectively (Videos S1 and S2; Supplemental information). Notably, the droplet exhibits an apparent directional motion on the inclined Janus structure. In brief, the droplet first exhibits a pancake bouncing at 4.3 ms, and then the droplet recoils and bounces along the direction of the pillars' orientation simultaneously. However, without an inclined angle, the lateral shift on vertical Janus structures is smaller under We = 51.6 (Figure 2B). A similar droplet oblique pancake bouncing is observed on inclined conical structures, while no noticeable displacement is found in its vertical version (Figure S5). Moreover, it is noted that the bouncing droplet is prone to break into two or three sub-droplets due to Rayleigh-Plateau instability on surfaces with conical structures. Figure 2C summarizes horizontal displacements x as a function of We on surfaces I–IV. For cases with the breakup of droplets, the displacement is calculated as $x = \sum_{i=1}^{j} m_i x_i / \sum_{i=1}^{j} m_i$, where m_i and x_i represent the mass and corresponding displacement for individual smaller satellite droplets, respectively. It is found that droplets on Janus structures show a larger lateral displacement than those on conical structures, regardless of We, for both vertical and inclined cases.

Data analysis and model building

We propose a simple analytical argument to illustrate the intriguing oblique pancake bouncing behaviors observed on Janus structures in comparison with conical structures. In consideration of pillar inclination and the intrinsic contact angle (CA) θ of water on the substrate material, the horizontal component of F_c on the left and right sides of the conical structure can be expressed as $F_{hL} \sim F_c \cos(\theta - \alpha_L)$ and $F_{hR} \sim -F_c \cos(\alpha_R + \theta)$, respectively. Therefore, the total horizontal force due to capillary effect for conical structures can be expressed as

$$F_{hCo} \sim \frac{\gamma R_b h_p D_0^2}{h d^2} [\cos(\theta - \alpha_L) + \cos(\theta + \alpha_R)], \quad (1)$$

where $\alpha_L = \arctan(1/\cot\beta - R_b/h)$ and $\alpha_R = \arctan(1/\cot\beta + R_b/h)$ ($0 < \alpha_R < \alpha_L < 180°$). For the Janus structure, $F_{hL} \sim F_c \cos(\theta - \beta)$ and $F_{hR} \sim -F_c \cos(\alpha_R + \theta)$, so the total horizontal force induced by capillary effect for Janus structures is given by
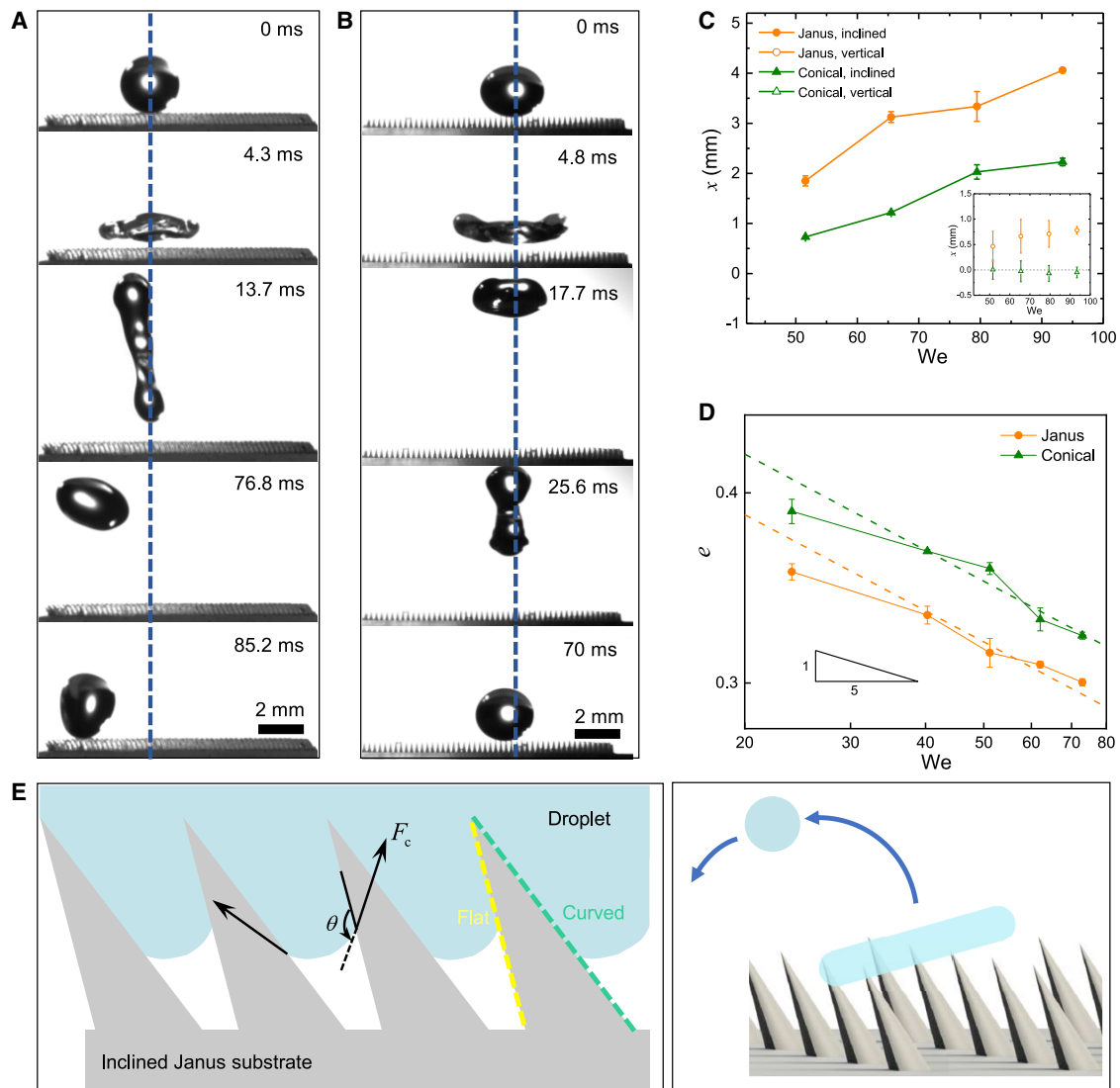
Figure 2. Droplet bouncing dynamics and the related quantitative measurement

(A and B) Selected snapshots of droplet bouncing on the Janus structure under We = 51.6 with (A) β = 70° and (B) β = 90°. The centerline of the droplet at the initial moment is denoted by a blue dashed line.

(C) Relation between the displacement x and the We for surfaces with conical and Janus structures.

(D) Restitution coefficient e as functions of We in a log-log plot.

(E) Schematic showing the capillary force on inclined Janus structures and the mechanism for the oblique pancake bouncing. The horizontal components of F_c on the flat side and the curved side are unbalanced, and thereby, we have a net horizontal force F_{hJa}. F_{hJa} works with F_{vJa}, together triggering a synchronized preferential droplet motion and pancake bouncing. All of the error bars are the SDs of the average values.

$$F_{hJa} \sim \frac{\gamma R_b h_P D_0^2}{hd^2}[cos(\theta - \beta) + cos(\theta + \alpha_R)]. \qquad (2)$$

Similarly, the vertical components of F_c for conical and Janus structures are expressed as

$$F_{vCo} \sim \frac{\gamma R_b h_P D_0^2}{hd^2}[sin(\theta - \alpha_L) - sin(\theta + \alpha_R)] \qquad (3)$$

and

$$F_{vJa} \sim \frac{\gamma R_b h_p D_0^2}{hd^2}[sin(\theta - \beta) - sin(\theta + \alpha_R)], \quad (4)$$

respectively.

Thus, it is obtained from the above analysis that for vertical cases with $\beta = 90°$, $F_{hCo} = 0$ while $F_{hJa} < 0$, which indicates that the vertical Janus structure is capable of imparting droplet preferential transport toward the flat side while the conical counterpart tends only to initiate vertical droplet bouncing. This is consistent with experimental results shown in Figures 2 and S5. Despite the observed directional motion of droplets on both Janus and conical structured samples, the characterized transport distances are distinct (Figure 2C). To rationalize the performance difference, we should refer to Equations (1) and (2). As $\beta < \alpha_L$, it is easy to obtain that $|F_{hCo}| < |F_{hJa}|$, which explains why the Janus structure shows a better performance than the conical structure in terms of liquid directional transport capability. Therefore, by integrating the Janus unit into the inclined pillars (i.e., $0 < \beta < 90°$), the capability of the droplet's directional motion is further enhanced.

To have a better understanding of how the surface morphology mediates the droplet impact behaviors, we further calculated the variation of the restitution coefficient e against We. Here, $e = v'/v$ is defined as the ratio of droplet bouncing velocity v' to the impact velocity v. As shown in Figure 2D, e decreases monotonically from ~0.4 to ~0.3 with the increasing of We, yet the descending line is affected by the surface morphology. Illustrating the function of e (We) in a log-log plot indicates that their relation can be expressed as $e \sim We^{-1/5}$. It is understood that the viscous dissipation in the shear boundary layer increases with Reynolds number Re. As Re increases with We for a given liquid, the descending trend of e with We might be explained by the increased viscous dissipation at an elevated We. This is also consistent with previous work,[41] for which the droplet impact becomes less elastic with the increasing of We within the range used in this work.

Based on Equations (1), (2), (3), and (4), the sample geometric parameters play important roles on the oblique pancake bouncing behavior. As a control experiment, we also fabricated samples with decreased pillar heights ($h = 100$ μm, 200 μm, and 300 μm) and reduced pillar density ($d = 400$ μm). On these control samples, the droplet exhibits conventional superhydrophobic bouncing (Figures S6 and S7) instead of the oblique pancake bouncing. The results suggest that the surface geometry needs to be delicately designed to generate the proper capillary force for initiating the distinct oblique pancake bouncing. To investigate the effect of surface wettability on droplet bouncing dynamics, we also conduct droplet impact experiments on superhydrophilic surfaces (CA < 5°) with inclined Janus structures. Instead of bouncing off, the impacting droplet spreads and penetrates the spacing of Janus pillars, and it eventually gets pinned on substrates. (Figure S8).

With the above information, we can summarize the whole bouncing behavior on the inclined Janus structure, as shown in Figure 2E. During the droplet impact process, the flow behavior is mainly regulated by the capillary force exerted by the periphery of pillars. Because of the inclination effect as well as the asymmetric Janus unit, the horizontal components of F_c on the flat side and the curved side of Janus structures are unbalanced; thereby, we have a net horizontal force F_{hJa} serving to initiate the directional motion. Moreover, the vertical component F_{vJa} works as the driving force for the pancake bouncing. In this case, F_{hJa} and F_{hJa} are united, altogether triggering a synchronized preferential droplet motion and pancake bouncing with a reduced contact time.
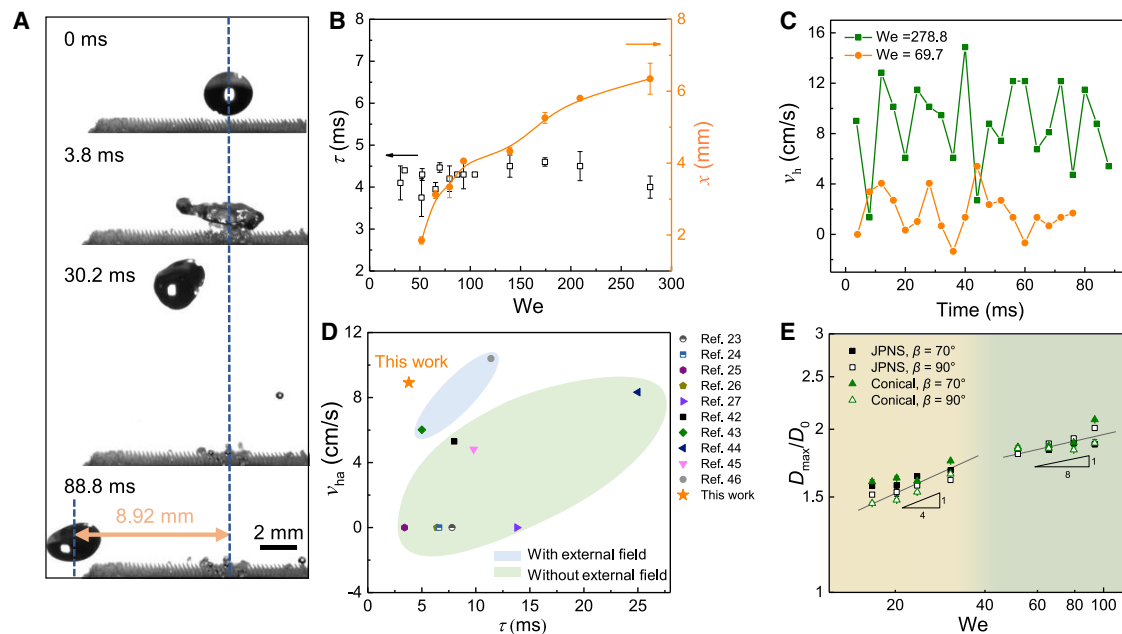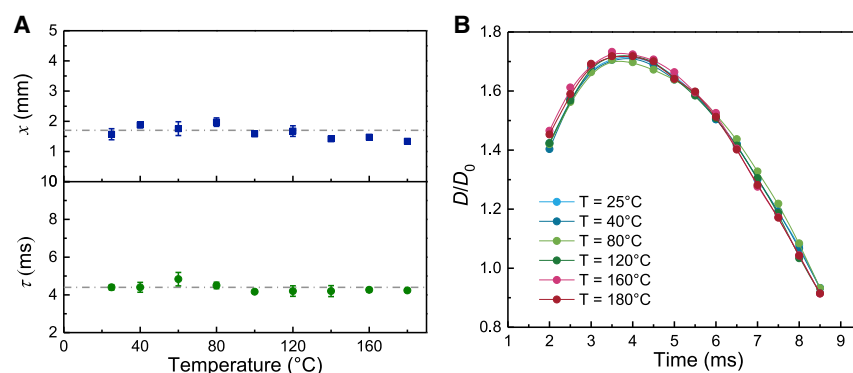
Figure 3. Oblique pancake bouncing dynamics under high We and the quantitative measurement of droplet dynamics within a broad range of We

(A) Representative snapshots of droplet oblique pancake bouncing on the inclined Janus structure under a high We = 278.8.

(B) Contact time τ and lateral displacement x as functions of We in the range of 30~280.

(C) The measured horizontal velocity v_h against time under We = 69.7 and 278.8.

(D) Comparison of the droplet bouncing dynamics in terms of the contact time τ and the average horizontal velocity v_{ha}. The green area represents the droplet bouncing on structured surface without any external actuation. The blue area denotes that the study requires external magnetic field stimuli. The orange star is the data of our work.

(E) The normalized maximum spreading diameter as a function of We. All of the error bars are the SDs of the average values.

Generality of oblique pancake bouncing

As the kinetic energy plays a vital role in affecting the outcome of droplet dynamics, we further perform droplet bouncing experiments on inclined Janus structures in a broader range of We conditions. As shown in Figures 3A and S9, splashing behavior is observed at high We conditions, where the original intact droplet disintegrates into satellite droplets. Despite the manifested splashing at high We, the drop still displays robust oblique pancake bouncing, as evidenced by both the reduced contact time and the preferential motion ability (Figure 3B). In addition, the measured horizontal velocity v_h is plotted against time under We = 69.7 and 278.8, as shown in Figure 3C. Specifically, for the case of We = 278.8, the average horizontal velocity v_{ha} is about 9 cm/s, which is around three times larger than that with We = 69.7. This, fortunately, gives us the flexibility to manipulate the oblique pancake bouncing behavior by varying the drop impact velocity. To illustrate the superiority of our surface design, we benchmark the contact time τ and the average horizontal velocity v_{ha} of a droplet in one bouncing cycle against those state-of-the-art structured surfaces, as shown in Figure 3D.[24–27,42–46] In striking contrast to the configurations without any external field (green area), our surface design outperforms other reported surfaces and demonstrates a remarkably synergic dominance in terms of τ and v_{ha}. Although one case with an external field (gray circle) shows a slightly (~20%) higher horizontal velocity, unfortunately, the required contact time is two times longer than ours. More importantly, the demand on external actuations makes the integration complex and brings reliability issues and, thus, limits their practicability applications. Therefore, our unique surface exhibits superior performance over other reported structured surfaces in literature. In

Figure 4. Oblique pancake bouncing under various thermal conditions with We = 34.9
(A) The displacement x and contact time τ as functions of temperature T.
(B) The temporal evolution of spreading diameters at different temperatures. The start point is from 2 ms because it is difficult to measure the contact line precisely when liquid rim is immersed into the space between pillars. All of the error bars are the SDs of the average values.

addition, the top-view images illustrate that the drop exhibits an obvious doughnut shape in the retraction process, where the rim zone of the droplet is thick while the central zone is thin (Figure S9). The distinct retraction dynamics implies that the pancake bouncing contributes to a redistribution of fluid momentum and mass, thus reshaping the droplet hydrodynamics. This is also evidenced by the scaling of D_{max}/D_0 versus We as shown in Figure 3E, for which $D_{max}/D_0 \sim We^{1/4}$ is found in the conventional rebound regime while it shifts to $D_{max}/D_0 \sim We^{1/8}$ in the pancake bouncing regime.

The generality of the oblique pancake bouncing on inclined Janus structures is further elucidated under various thermal conditions with temperatures ranging from 25°C to 180°C. Normally, the liquid surface tension decreases, provided it is in contact with a hot substrate, and thereby both F_{hJa} and F_{vJa} would be decreased based on Equations (2) and (4). In other words, the biased motion and the pancake bouncing might be lessened or even eliminated at high temperatures. Unexpectedly, as shown in Figure 4A, it is found that both the displacement x and the contact time τ are independent of temperature on the inclined Janus structure, which ensures a robust water repellency and drop motion directionality. The time evolution of contact line dynamics at different temperatures is characterized in Figure 4B. Consistent with the results in Figure 4A, the influence of temperature is negligible. The irrelevance on temperature is attributed to the extremely short contact time, which limits the heat transfer from the solid to the liquid. This may offer us opportunities for applications in thermal devices.

In conclusion, by taking advantage of the inclined Janus structure, the pancake bouncing and the directional transportation are realized synchronously in one rebounding cycle, which facilitates a rapid droplet removal. The driven forces of this intriguing motion are found to be the vertical and horizontal components of the capillary force, exerted by the periphery of inclined pillars. Furthermore, the robust water repellency and liquid motion directionality are examined under various thermal conditions and different impact velocities. From a broader perspective, our work will provide important insights into the evolutionary development of liquid manipulation and might find promising applications in the field requiring directional rapid liquid detachment, such as anti-icing, self-cleaning, and electricity generation.

EXPERIMENTAL PROCEDURES

Resource availability

Lead contact

Further information and requests for resources and procedures should be directed to the lead contact, Dr. Chonglei Hao (haoc@hit.edu.cn).

Materials availability

All unique surfaces generated in this study are available from the lead contact without restriction.

Data and code availability

All of the data supporting the findings of this study are presented within the article and supplemental information. All other data are available from the lead contact upon reasonable request.

Sample fabrication

Samples were constructed by a projection microstereolithography-based 3D printing technique (BMF Precision Tech, nanoArch S140). In the fabrication, a model, which was prebuilt by a mapping software, was sliced into a series of 2D images. Subsequently, an exposure process was performed. The whole steps were iterated for each layer until the designed structure was created. To render surfaces' superhydrophobicity, substrates were silanized with the assistance of a hydrogen-bond-driven technique and coated with nanoparticles. Specifically, the samples were treated in a 1-mM hexane solution of trichloro (1H,1H,2H,2H-perfluorooctyl) silane for 30 min and then were placed on a hot plate at 80°C for 30 min in air. In the following, the surface was spray coated by a nanoparticle-dispensed solution (Glaco, Soft 99). Finally, the samples were heated at 60°C for 20 min to complete drying. In addition, a conventional superhydrophobic surface was fabricated via coating nanoparticles on a glass slide, and a superhydrophilic surface with inclined Janus structures is made by spray coating a superhydrophilic film (Anti-fog coating, Bluechem) to test the effect of surface wettability on droplet bouncing dynamics.

Wettability characterization

To characterize the surface wettability, CAs of surface I–VIII were measured by a CA goniometer (Dataphysics Instrument OCA 25) at room temperature, and the results are shown in Figure S10. Static CAs on surfaces I–IV are in the range of 140° to 150°, illustrating a non-wetting property. Sliding angles on surfaces I–IV are within 5°, indicating a high droplet mobility. For surfaces V–VIII, the static CA is lower (120° to 140°), and the sliding angle is higher (within 17°), owing to a larger spacing compared to those of surfaces I–IV.

Droplet impact experiment

The whole apparatus was placed on a vibration isolation table. The cold light was provided by two LED lamps. The deionized water droplet with a diameter D_0 of 2.56 mm was generated by a flat-tip stainless steel needle, which was connected to a plastic 10-mL syringe and a syringe pump (LSP01-3A) via a rubber tube, from a pre-determined height. By adjusting the height of the needle, the droplet impact velocity could be varied. With the propulsion of the syringe, the droplet forms at the needle tip, grows in size, and finally detaches once its weight overwhelms the attraction force caused by the surface tension. Two high-speed cameras (Photron FASTCAM Nova S12 and Mini AX200) were employed to make synchronized recordings of the droplet impingement dynamics from the side and high-angle views at a frame rate of 10,000 fps with a shutter speed of 1/10,000 s. A hot plate (Thermo

Scientific Super-Nuova) was used to control the temperature of samples. The image analysis was conducted by the software ImageJ. The horizontal velocity v_h is calculated by comparing the centroid motion of the droplet between adjacent frames with an interval of 4 ms. All the experiments were carried out in an ambient environment at room temperature.

SUPPLEMENTAL INFORMATION

Supplemental information can be found online at https://doi.org/10.1016/j.xcrp.2021.100721.

AUTHOR CONTRIBUTIONS

C.H. conceived the initial idea for this research. B.L. and C.H. supervised the research. R.T., G.L., B.D., and J.W. performed the experiments. R.T., G.L., and C.H. carried out the theoretical analysis. R.T. and C.H. were responsible for writing the paper. All authors have given approval to the final version of the manuscript.

DECLARATION OF INTERESTS

The authors declare no competing interests.

REFERENCES

1. Joung, Y.S., Ge, Z., and Buie, C.R. (2017). Bioaerosol generation by raindrops on soil. Nat. Commun. *8*, 14668.

2. Kim, S., Wu, Z., Esmaili, E., Dombroskie, J.J., and Jung, S. (2020). How a raindrop gets shattered on biological surfaces. Proc. Natl. Acad. Sci. USA *117*, 13901–13907.

3. Kim, J. (2007). Spray cooling heat transfer: The state of the art. Int. J. Heat Fluid Flow *28*, 753–767.

4. Fernández-Toledano, J.C., Braeckeveldt, B., Marengo, M., and De Coninck, J. (2020). How wettability controls nanoprinting. Phys. Rev. Lett. *124*, 224503.

5. Foresti, D., Kroll, K.T., Amissah, R., Sillani, F., Homan, K.A., Poulikakos, D., and Lewis, J.A. (2018). Acoustophoretic printing. Sci. Adv. *4*, eaat1659.

6. Xu, W., Zheng, H., Liu, Y., Zhou, X., Zhang, C., Song, Y., Deng, X., Leung, M., Yang, Z., Xu, R.X., et al. (2020). A droplet-based electricity generator with high instantaneous power density. Nature *578*, 392–396.

7. Josserand, C., and Thoroddsen, S.T. (2016). Drop impact on a solid surface. Annu. Rev. Fluid Mech. *48*, 365–391.

8. Yarin, A.L. (2006). Drop impact dynamics: splashing, spreading, receding, bouncing…. Annu. Rev. Fluid Mech. *38*, 159–192.

9. Si, Y., Hu, J., and Dong, Z. (2021). Bioinspired magnetically driven liquid manipulation as microrobot. Cell Rep. Phys. Sci. *2*, 100439.

10. Lu, Y., Sathasivam, S., Song, J., Crick, C.R., Carmalt, C.J., and Parkin, I.P. (2015). Repellent materials. Robust self-cleaning surfaces that function when exposed to either air or oil. Science *347*, 1132–1135.

11. Geyer, F., D'Acunzi, M., Sharifi-Aghili, A., Saal, A., Gao, N., Kaltbeitzel, A., Sloot, T.-F., Berger, R., Butt, H.-J., and Vollmer, D. (2020). When and how self-cleaning of superhydrophobic surfaces works. Sci. Adv. *6*, eaaw9727.

12. Wang, D., Sun, Q., Hokkanen, M.J., Zhang, C., Lin, F.-Y., Liu, Q., Zhu, S.-P., Zhou, T., Chang, Q., He, B., et al. (2020). Design of robust superhydrophobic surfaces. Nature *582*, 55–59.

13. Ghosh, A., Beaini, S., Zhang, B.J., Ganguly, R., and Megaridis, C.M. (2014). Enhancing dropwise condensation through bioinspired wettability patterning. Langmuir *30*, 13103–13115.

14. Boreyko, J.B., and Chen, C.-H. (2009). Self-propelled dropwise condensate on superhydrophobic surfaces. Phys. Rev. Lett. *103*, 184501.

15. Wu, H., Mendel, N., van den Ende, D., Zhou, G., and Mugele, F. (2020). Energy harvesting from drops impacting onto charged surfaces. Phys. Rev. Lett. *125*, 078301.

16. Mouterde, T., Lehoucq, G., Xavier, S., Checco, A., Black, C.T., Rahman, A., Midavaine, T., Clanet, C., and Quéré, D. (2017). Antifogging abilities of model nanotextures. Nat. Mater. *16*, 658–663.

17. Yang, S., Wu, C., Zhao, G., Sun, J., Yao, X., Ma, X., et al. (2021). Condensation frosting and passive anti-frosting. Cell Rep. Phys. Sci. *2*, 100474.

18. Liao, D., He, M., and Qiu, H. (2019). High-performance icephobic droplet rebound surface with nanoscale doubly reentrant structure. Int. J. Heat Mass Transf. *133*, 341–351.

19. Maitra, T., Tiwari, M.K., Antonini, C., Schoch, P., Jung, S., Eberle, P., and Poulikakos, D. (2014). On the nanoengineering of superhydrophobic and impalement resistant surface textures below the freezing temperature. Nano Lett. *14*, 172–182.

20. Richard, D., Clanet, C., and Quéré, D. (2002). Contact time of a bouncing drop. Nature *417*, 811.

21. Okumura, K., Chevy, F., Richard, D., Quéré, D., and Clanet, C. (2003). Water spring: A model for bouncing drops. Europhys. Lett. *62*, 237–243.

22. Hao, C., Liu, Y., Chen, X., Li, J., Zhang, M., Zhao, Y., and Wang, Z. (2016). Bioinspired Interfacial Materials with Enhanced Drop Mobility: From Fundamentals to Multifunctional Applications. Small *12*, 1825–1839.

23. Bird, J.C., Dhiman, R., Kwon, H.M., and Varanasi, K.K. (2013). Reducing the contact time of a bouncing drop. Nature *503*, 385–388.

24. Chantelot, P., Mazloomi Moqaddam, A., Gauthier, A., Chikatamarla, S.S., Clanet, C., Karlin, I.V., and Quéré, D. (2018). Water ring-bouncing on repellent singularities. Soft Matter *14*, 2227–2233.

25. Liu, Y., Moevius, L., Xu, X., Qian, T., Yeomans, J.M., and Wang, Z. (2014). Pancake bouncing on superhydrophobic surfaces. Nat. Phys. *10*, 515–519.

26. Gauthier, A., Symon, S., Clanet, C., and Quéré, D. (2015). Water impacting on superhydrophobic macrotextures. Nat. Commun. *6*, 8001.

27. Wang, L., Wang, R., Wang, J., and Wong, T.-S. (2020). Compact nanoscale textures reduce contact time of bouncing droplets. Sci. Adv. *6*, eabb2307.

28. Tao, R., Ng, T., Su, Y., and Li, Z. (2020). A microfluidic rectifier for Newtonian fluids using asymmetric converging–diverging microchannels. Phys. Fluids *32*, 052010.

29. Lagubeau, G., Le Merrer, M., Clanet, C., and Quéré, D. (2011). Leidenfrost on a ratchet. Nat. Phys. *7*, 395–398.

30. Lv, J.A., Liu, Y., Wei, J., Chen, E., Qin, L., and Yu, Y. (2016). Photocontrol of fluid slugs in liquid crystal polymer microactuators. Nature *537*, 179–184.

31. Sun, Q., Wang, D., Li, Y., Zhang, J., Ye, S., Cui, J., Chen, L., Wang, Z., Butt, H.-J., Vollmer, D., and Deng, X. (2019). Surface charge printing for programmed droplet transport. Nat. Mater. *18*, 936–941.

32. Bjelobrk, N., Girard, H.-L., Subramanyam, S.B., Kwon, H.-M., Quere, D., and Varanasi, K.K. (2016). Thermocapillary motion on lubricant-impregnated surfaces. Phys. Rev. Fluids *1*, 063902.

33. Chen, H., Zhang, P., Zhang, L., Liu, H., Jiang, Y., Zhang, D., Han, Z., and Jiang, L. (2016). Continuous directional water transport on the peristome surface of Nepenthes alata. Nature *532*, 85–89.

34. Comanns, P., Buchberger, G., Buchsbaum, A., Baumgartner, R., Kogler, A., Bauer, S., and Baumgartner, W. (2015). Directional, passive liquid transport: the Texas horned lizard as a model for a biomimetic 'liquid diode'. J. R. Soc. Interface *12*, 20150415.

35. Dai, H., Dong, Z., and Jiang, L. (2020). Directional liquid dynamics of interfaces with superwettability. Sci. Adv. *6*, eabb5528.

36. Yan, X., Jin, Y., Chen, X., Zhang, C., Hao, C., and Wang, Z. (2019). Nature-inspired surface topography: design and function. Sci. China Phys. Mech. *63*, 1–15.

37. Feng, S., Delannoy, J., Malod, A., Zheng, H., Quéré, D., and Wang, Z. (2020). Tip-induced flipping of droplets on Janus pillars: From local reconfiguration to global transport. Sci. Adv. *6*, eabb4540.

38. Lv, C., Chen, C., Chuang, Y.-C., Tseng, F.-G., Yin, Y., Grey, F., and Zheng, Q. (2014). Substrate curvature gradient drives rapid droplet motion. Phys. Rev. Lett. *113*, 026101.

39. Chu, K.-H., Xiao, R., and Wang, E.N. (2010). Unidirectional liquid spreading on asymmetric nanostructured surfaces. Nat. Mater. *9*, 413–417.

40. McCarthy, M., Gerasopoulos, K., Enright, R., Culver, J.N., Ghodssi, R., and Wang, E.N. (2012). Biotemplated hierarchical surfaces and the role of dual length scales on the repellency of impacting droplets. Appl. Phys. Lett. *100*, 263701.

41. Biance, A.L., Chevy, F., Clanet, C., Lagubeau, G., and Quéré, D. (2006). On the elasticity of an inertial liquid shock. J. Fluid Mech. *554*, 47–66.

42. Li, P., Xu, X., Yu, Y., Wang, L., and Ji, B. (2021). Biased Motions of a Droplet on the Inclined Micro-conical Superhydrophobic Surface. ACS Appl. Mater. Interfaces *13*, 27687–27695.

43. Wang, L., Gao, C., Hou, Y., Zheng, Y., and Jiang, L. (2016). Magnetic field-guided directional rebound of a droplet on a superhydrophobic flexible needle surface. J. Mater. Chem. A Mater. Energy Sustain. *4*, 18289–18293.

44. Li, D., Feng, S., Xing, Y., Deng, S., Zhou, H., and Zheng, Y. (2017). Directional bouncing of droplets on oblique two-tier conical structures. RSC Advances *7*, 35771–35775.

45. Wang, S., Li, H., Duan, H., Cui, Y., Sun, H., Zhang, M., Zheng, X., Song, M., Li, H., Dong, Z., et al. (2020). Directed motion of an impinging water droplet—seesaw effect. J. Mater. Chem. A Mater. Energy Sustain. *8*, 7889–7896.

46. Lee, S.H., Seong, M., Kwak, M.K., Ko, H., Kang, M., Park, H.W., Kang, S.M., and Jeong, H.E. (2018). Tunable multimodal drop bouncing dynamics and anti-Icing performance of a magnetically responsive hair array. ACS Nano *12*, 10693–10702.